Defect-Induced Hedgehog Polarization States in Multiferroics

Linze Li,[1,2] Xiaoxing Cheng,[3] Jacob R. Jokisaari,[2] Peng Gao,[2] Jason Britson,[3] Carolina Adamo,[4] Colin Heikes,[4] Darrell G. Schlom,[4,5] Long-Qing Chen,[3] and Xiaoqing Pan[1,6,*]

[1]*Department of Chemical Engineering and Materials Science, University of California–Irvine, Irvine, California 92697, USA*
[2]*Department of Materials Science and Engineering, University of Michigan, Ann Arbor, Michigan 48109, USA*
[3]*Department of Materials Science and Engineering, Penn State University, University Park, Pennsylvania 16802, USA*
[4]*Department of Materials Science and Engineering, Cornell University, Ithaca, New York 14853, USA*
[5]*Kavli Institute at Cornell for Nanoscale Science, Ithaca, New York 14853, USA*
[6]*Department of Physics and Astronomy, University of California–Irvine, Irvine, California 92697, USA*

(Received 27 October 2017; published 27 March 2018)

Continuous developments in nanotechnology require new approaches to materials synthesis that can produce novel functional structures. Here, we show that nanoscale defects, such as nonstoichiometric nanoregions (NSNRs), can act as nano-building blocks for creating complex electrical polarization structures in the prototypical multiferroic $BiFeO_3$. An array of charged NSNRs are produced in $BiFeO_3$ thin films by tuning the substrate temperature during film growth. Atomic-scale scanning transmission electron microscopy imaging reveals exotic polarization rotation patterns around these NSNRs. These polarization patterns resemble hedgehog or vortex topologies and can cause local changes in lattice symmetries leading to mixed-phase structures resembling the morphotropic phase boundary with high piezoelectricity. Phase-field simulations indicate that the observed polarization configurations are mainly induced by charged states at the NSNRs. Engineering defects thus may provide a new route for developing ferroelectric- or multiferroic-based nanodevices.

DOI: 10.1103/PhysRevLett.120.137602

Quasi-1D ferroic states arising from the interplay of spin, charge, orbital, and/or lattice degrees of freedom in strongly correlated oxides usually exhibit complex polarization or spin textures and unique properties that hold great promise for the development of new device paradigms [1]. Examples include vortices, hedgehogs, and Skyrmions that have been discovered and extensively studied in magnetic materials [2–4]. These magnetic states can be efficiently manipulated by magnetic fields [5,6] or driven by a spin-transfer torque at ultralow current densities [7] and thus can be potentially applied for high-density magnetic memories or current-driven devices. At the same time, considerable interest has also been given to exploring new polarization states in ferroelectrics, because the use of ferroelectric states that are much smaller than their counterparts in magnets as functional elements in nanodevices is particularly attractive. For example, advances in the synthesis of ferroelectric thin-film heterostructures have enabled the creation of periodic patterns of polarization vortices through tuning the boundary conditions at film interfaces [8–10]. It is also theoretically predicted that Skyrmion-like polarization patterns can be stabilized in ferroelectric nanocomposites through the application of external electric fields [11]. Yet, another type of quasi-1D ferroelectric state known as the polarization hedgehog, in which all the polarization vectors diverge from the center of the structure, remains relatively unexplored. This is partially because such a hedgehog state is generally considered unstable, unless the inevitable accumulation of a large amount of polarization bound charge at the center of the structure can be compensated by some strong driving force. An intriguing theoretical work has predicted that the hedgehog states can be stabilized in $BaTiO_3$ nanowires under specific boundary conditions, where surface effects play a critical role [12]. But these hedgehog states have not yet been experimentally confirmed.

On the other hand, the recent observation of a strong interaction between ferroelectric polarization and built-in fields induced by charged impurity defects embedded in the ferroelectric matrix suggests that these defects may be used as nano-building blocks that can provide a strong electrostatic-driven force for stabilization of complex domain structures [13,14]. For example, it has been shown that nanoscale planar charged defects in $BiFeO_3$ thin films can induce novel head-to-head mixed-phase polarization structures [13]. Nevertheless, these observed impurity defects were accidentally introduced in those films, and the possiblity to precisely control the formation of the defects and thus to generate the desired domain structures has not been studied. Here, we show that, by controlling the substrate temperature during the growth of a $BiFeO_3$ thin film, an array of nonstoichiometric nanoregions (NSNRs) can be deliberately introduced as charged defects into the host material matrix, which leads to the stabilization of novel hedgehog or antihedgehog nanodomains. These

nanodomains present exotic patterns of polarization rotation that form mixed-phase structures and can be coupled with polarization vortices. Their novel properties could be useful for nanoelectronic and electromechanical applications.

$BiFeO_3$ is a room-temperature multiferroic with a rhombohedral lattice structure, exhibiting coupled ferroelectric ($T_C \sim 1103$ K) and antiferromagnetic ($T_N \sim 650$ K) order [15]. In pseudocubic unit cells [Fig. 1(a)], the oxygen octahedra and the central Fe cation are displaced from their respective positions at the face and body centers, giving rise to a large spontaneous polarization ($\sim 100\ \mu C\,cm^{-2}$) along the $\langle 111 \rangle_{PC}$ directions [15–19], where the PC subscript represents pseudocubic indices. Using aberration-corrected high-angle annular dark-field (HAADF) scanning transmission electron microscopy (STEM) imaging, the atomic-scale structure within a $BiFeO_3$ thin film can be directly visualized, and the polarization vector within each pseudocubic unit cell can be measured. For example, in the HAADF image shown in Fig. 1(b), where the Bi columns appear as the brighter dots, the Fe columns show weaker contrast, and the oxygen atoms are not visible, a vector, $\boldsymbol{D_{FB}}$, can be defined as the atomic displacement in the image plane of the Fe cation from the center of the unit cell formed by its four Bi neighbors. This $\boldsymbol{D_{FB}}$ vector is exactly opposite to the projection of the polarization vector in the image plane and can be directly measured by fitting the atomic columns as two-dimensional (2D) Gaussian peaks to locate their centers and recording the offset [8,20].

The growth of $BiFeO_3$ films is very sensitive to deposition parameters, and by most deposition techniques phase-pure $BiFeO_3$ can be obtained only within a narrow combination of growth parameters [21]. An alternate

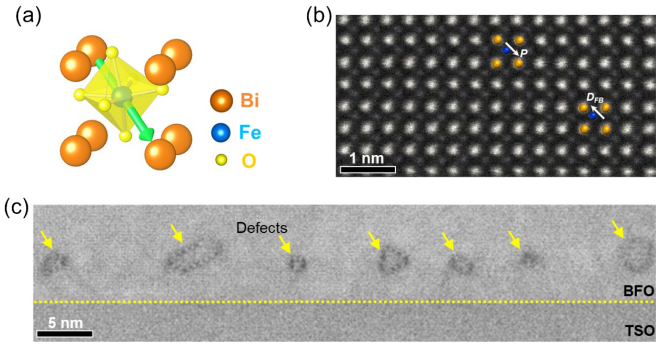

FIG. 1. Atomic structure and defects in a $BiFeO_3$ thin film. (a) Atomic model of the pseudocubic structure of $BiFeO_3$. Polarization is shown by a green arrow. (b) HAADF STEM image of a $BiFeO_3$ thin film viewed in cross section along the $[100]_{PC}$ zone axis. The $\boldsymbol{D_{FB}}$ vector, defined as the atomic displacement in the image plane of the Fe cation from the center of the unit cell formed by its four Bi neighbors, is opposite to the polarization vector ($\boldsymbol{P}$). (c) HAADF STEM image of the $BiFeO_3$(BFO)/$TbScO_3$(TSO) interfacial region, where the interface is indicated by the yellow dashed line and an array of defects are observed at a uniform height of 3 nm above the interface.

method enabling the growth of phase-pure $BiFeO_3$ for a broader range of growth parameters, referred to as the "growth window," is what we use when synthesizing $BiFeO_3$ by molecular-beam epitaxy (MBE). In this process, $BiFeO_3$ is formed by flooding the growing film with excess bismuth and oxidant and relying on thermodynamics to desorb the excess of both of these constituents, resulting in a phase-pure $BiFeO_3$ film for conditions within the growth window. Our prior MBE work mapping out the adsorption-controlled growth conditions for $BiFeO_3$ indicates that a change of the substrate temperature during film growth, given a constant bismuth and oxygen overpressure at a fixed Bi:Fe flux ratio, can result in three different products: (I) $BiFeO_3 + \gamma\text{-}Fe_2O_3$ (at a higher than optimal temperature), (II) $BiFeO_3$ (within the growth window, i.e., at an optimal temperature), and (III) $BiFeO_3 + Bi_2O_{2.5}$ (at a lower than optimal temperature) [22]. The formation of the Fe-rich or Bi-rich defects can be directly monitored during film growth by *in situ* RHEED, since these defects can generate additional spots in the RHEED pattern [22].

In this work, we grew epitaxial $(001)_{PC}$-oriented $BiFeO_3$ thin films on $(110)_O$ $TbScO_3$ single crystal substrates (where the O subscript represents orthorhombic indices) by MBE, monitoring the growth by RHEED. The films were grown at constant bismuth (Bi flux $= 1.4 \times 10^{14}$ Bi/cm^2 s) and oxygen ($O_2 + \sim 10\%$ O_3 background pressure $= 1 \times 10^{-6}$ Torr) with pressure over a fixed Bi:Fe flux ratio of 8:1. Film growth was initiated at a substrate temperature of $\sim 680\,^{\circ}C$ (higher than the optimal temperature) until additional spots in the RHEED pattern, indexed to diffraction from (111)-oriented $\gamma\text{-}Fe_2O_3$, were observed (Supplemental Fig. S1 [23]) [22]. Upon seeing these spots, the substrate temperature was decreased to $610\,^{\circ}C$ and the RHEED pattern, which is very surface sensitive, went back to that of phase-pure $BiFeO_3$. As a result, an array of Fe-rich defects were inserted into the $BiFeO_3$ matrix at a uniform height along the film thickness, several unit cells above the bottom interface of the film, evident in the HAADF STEM image shown in Fig. 1(c). In this way, control of the temperature lends control of the placement of defects in the film.

The atomic-scale structure of the defects is examined in Fig. 2(a), where a magnified HAADF image of an interfacial region containing one typical semicircular loop defect in the $BiFeO_3$ matrix is shown. As there are no other elements introduced during film growth, the defect should also be composed of Bi, Fe, and O atoms, with the brighter dots in the HAADF image corresponding to the heavier Bi columns and the weaker dots corresponding to the lighter Fe columns. This defect is generally composed of two parts. The first part is a short vertical segment on the right (highlighted in brown) with a distorted pseudocubic perovskite lattice, where an apparent lattice expansion is observed along the horizontal direction. The second part is a long curved or inclined segment on the left (highlighted

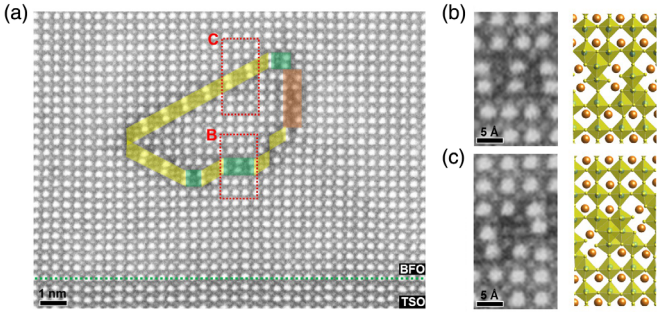

FIG. 2. Atomic structure associated with a semicircular loop defect in the $BiFeO_3$ thin film. (a) HAADF STEM image of the $BiFeO_3$(BFO)/$TbScO_3$(TSO) interfacial region containing one typical semicircular loop defect. The defect is composed of a vertical segment (highlighted in brown) with distorted pseudocubic perovskite lattices and nonstoichiometric planar (highlighted in green) and stepped (highlighted in yellow) structural units. (b) Magnified image of the nonstoichiometric planar unit in the defect [red rectangular highlighted region "B" in (a)] and a model of its corresponding atomic structure on the right. (c) Magnified image of the nonstoichiometric stepped unit in the defect [red rectangular highlighted region "C" in (a)] and a model of its corresponding atomic structure on the right.

in yellow and green) with a structure and stoichiometry different from the $BiFeO_3$ matrix, forming NSNRs. Furthermore, these NSNRs in the defect are composed from two structural units—planar units (highlighted in green) and stepped units (highlighted in yellow). While the planar unit is oriented on the horizontal $(001)_{PC}$ plane of $BiFeO_3$ and adopts the structure of one pair of Bi atoms alternating with one pair of Fe atoms, the stepped unit has an inclined orientation and is formed from one pair of Bi atoms alternating with two pairs of Fe atoms.

The same types of planar and stepped NSNRs have also been observed in previous studies of Nd- and Ti-doped antiferroelectric $BiFeO_3$ by MacLaren *et al.* [24,25]. Their detailed structural study suggests that the Fe atoms within the NSNRs are coordinated by six oxygens in the form of edge-sharing oxygen octahedra, resembling the structure of γ-Fe_2O_3 and forming the planar and stepped structural units shown schematically in Figs. 2(b) and 2(c), respectively. As a result, there is an excess of anions (more oxygen) at the NSNRs, which produces a net local negative charge density. Assuming Bi^{3+}, Fe^{3+}, and O^{2-} at the defects, the charge density is calculated to be -1.4 C/m^2 at the planar unit and -1.1 C/m^2 at the stepped unit. Another feature associated with the NSNRs is an atomic shift of one-half of a pseudocubic unit cell of the $BiFeO_3$ lattice across the planar units in the $[001]_{PC}$ direction and a shift of one-half of a pseudocubic unit cell of the $BiFeO_3$ lattice across the stepped units in both the $[010]_{PC}$ and $[001]_{PC}$ directions, as evident in the Fourier-filtered images shown in Supplemental Fig. S3 [23]. These shifts, however, do not induce obvious strain in the $BiFeO_3$ matrix, as shown by the quantitative analysis of the high-resolution HAADF images using geometric phase analysis (GPA) in Supplemental Fig. S4 [23]. The shift in the lattice occurs mainly through atomic rearrangement at the boundary of the NSNRs and the shifted $BiFeO_3$ lattices are separated, accommodating the strain and forming an isolated region enclosed by the loop defect.

The polarization distribution in the $BiFeO_3$ lattice adjacent to the defect was determined by mapping the $-\boldsymbol{D}_{FB}$ vectors [Fig. 3(a)]. Within the region enclosed by the semicircular defect (marked as region "1"), a hedgehog polarization state can be identified. While the polarization vectors of each unit cell in the middle of this region are attenuated and oriented along multiple directions, the unit cells that are in contact with the defect forming the periphery of the NSNRs (the unit cells highlighted by red rectangles) show significant lattice distortions with enhanced polarization pointing outward, towards the

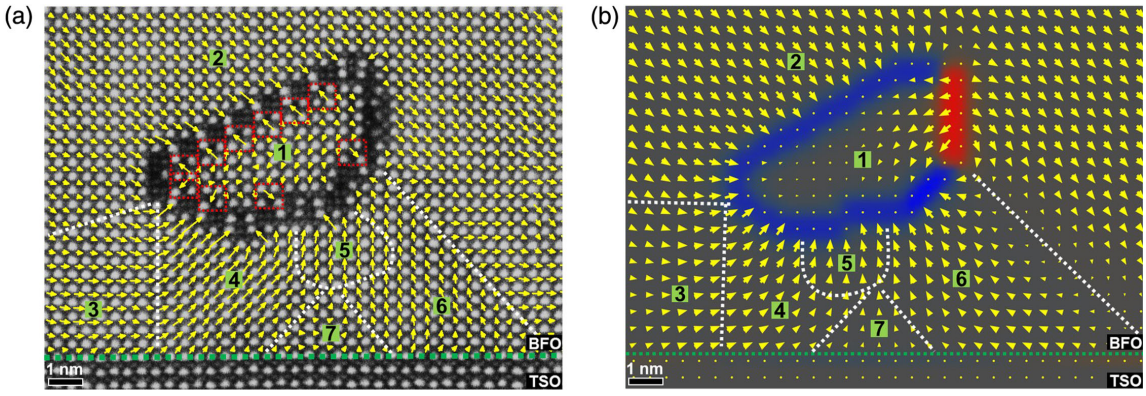

FIG. 3. Polarization map of the nanodomains surrounding the semicircular loop defect in the $BiFeO_3$ thin film. (a) The same HAADF STEM image as Fig. 2(a) overlaid with the polarization vectors ($-\boldsymbol{D}_{FB}$, shown by yellow arrows). The white dashed lines represent the positions of domain walls. (b) Phase field simulation of the polarization distribution in the image plane of the domain structure stabilized by a charged defect with a configuration similar to the experimental observation. The polarization vectors are overlaid on a color map of the charge distribution, where the red, blue, and gray colors represent positive (+1.1 C/m^2), negative (−1.1 C/m^2), and zero charge densities, respectively.

NSNRs. In contrast, the $BiFeO_3$ lattice outside of the defect presents a continuous rotation of polarization, with polarization vectors generally pointing inward towards the defect, except for the right-side region where the polarization vectors are pointing outward. This arrangement leads to the formation of six different nanodomains [marked "2"–"7" in Fig. 3(a)] surrounding the defect. Some of these domains also experience a change in lattice symmetry, forming mixed-phase structures. Particularly, the "2," "4," and "6" domains possess normal *rhombohedral-like* (*R*-like) structures with polarizations oriented along the diagonal directions. In contrast, the "3" and "5" domains adopt polarizations along $[010]_{PC}$ and $[001]_{PC}$ directions, respectively, resembling horizontal or vertical *tetragonal-like* (*T*-like) structures [26]. Within region 7, significantly attenuated polarizations were observed.

Since the polarization directions are generally pointing toward the NSNRs in the defect and these NSNRs are negatively charged, a plausible mechanism is that the polarization distortions of the $BiFeO_3$ lattices are modified by the built-in fields induced by the charge on the NSNRs. To gain further insight of the driving force for the formation of the nanodomains, we employ phase field simulations to calculate the stable polarization configuration in the presence of a charged defect. In the simulated $BiFeO_3$ thin film, we created a defect with a similar shape to what we observed in the experiment in Fig. 2 and then applied an additional charge at the defect, with no additional eigenstrain introduced by the defect from the lattice mismatch between the defect and the matrix, as the defect-induced strain has a minimal effect on the polarization (see Supplemental Material [23] for a discussion). Since the left curved or inclined part of the defect is mostly composed of the stepped units, for simplicity a uniform charge density of $-1.1\ C/m^2$ was applied there. Although the defect chemistry of the vertical segment on the right side of the defect cannot be directly determined by STEM imaging, its lattice expansion along the horizontal direction could indicate a local accumulation of oxygen vacancies and thus a positive charge density [27,28]. Simulations allow the effect of charge density to be studied, and a comparison of simulated results with different values of charge densities ranging from -1.1 to $+5.5\ C/m^2$ at the right-side segment of the defect is shown in Supplemental Fig. S5 [23]. The result with a charge density of $+1.1\ C/m^2$ [Fig. 3(b)] is most consistent with the experimental observation, indicating that the existence of a moderate positive charge is the most probable situation. Note that in each case a random polarization distribution was set as the initial structure, and simulations repeated with different initial random polarization distributions were found to yield consistent final configurations.

In the simulated polarization configuration around the defect [Fig. 3(b)], attenuated polarization is observed within the semicircular region enclosed by the defect (region 1), with the exception of the very large polarization of a few unit cells at the region boundary. This could be a result of the exclusion of the experimentally observed distorted unit cells at the region boundary [red rectangular highlighted unit cells in Fig. 3(a)] from the simulation. Nevertheless, the simulated results reproduced almost all of the features in the polarization configuration outside of the defect captured in the experiment, including the polarization reorientation around the defect with the formation of six different polarized regions (regions 2–7), the change of lattice symmetries into *T*-like structures in region 3 and 5, and the attenuated polarization in region 7. These results indicate that the charge on the NSNRs should be the major driving force inducing the observed nanodomain structures, in which the gradient energy from the polarization rotation is counterbalanced by the corresponding reduction in overall electrostatic energy.

The hedgehog and antihedgehog domains are ubiquitous around the defects composed of NSNRs in the $BiFeO_3$ thin films, and they can also induce polarization vortices, as shown by three examples in Figs. 4(a)–4(c). Similar to the previous case shown in Fig. 2, these defects are mainly comprised of the same types of nonstoichiometric planar units and stepped units, with the same excess of oxygen and thus local net negative charge. Some additional variations were noted. For example, within the circular defect in Fig. 4(a), an inclined segment is observed on the right side. It is composed of five consecutive pairs of Fe atoms with no Bi atoms in between them. Examination of the polarization shows that the hedgehog and antihedgehog domains around the defects are also accompanied by the formation of multiple different polarized regions and mixed-phase structures. In Fig. 4(a), a tiny hedgehog polarization state with a diameter of 4 unit cells was observed within the nanoregion encircled by the defect. In both Figs. 4(a) and 4(b), antihedgehog polarization states are stabilized at the shell regions surrounding the defects. On larger length scales outside of these defects, the overall continuous polarization rotation patterns lead to flux-closure vortex structures. In Fig. 4(c), a pair of polarization semivortex and semiantivortex structures form at the left and right sides of this nearly linear defect as a result of the formation of a "head-to-head" polarization configuration above and below the defect.

In conclusion, we have demonstrated the stabilization of novel hedgehog and antihedgehog nanodomains in multiferroic $BiFeO_3$ thin films by making use of nanoscale charged defects. These nanodomains offer new opportunities to explore the complex interplay of spin, charge, orbital, and lattice degrees of freedom in systems with strong electron correlations. As the hedgehog states are confined within the nanosized structure defects, they can approach sizes down to several unit cells and have a much higher density than the bulk domains in the film. Our finding therefore opens the door for creating high-density

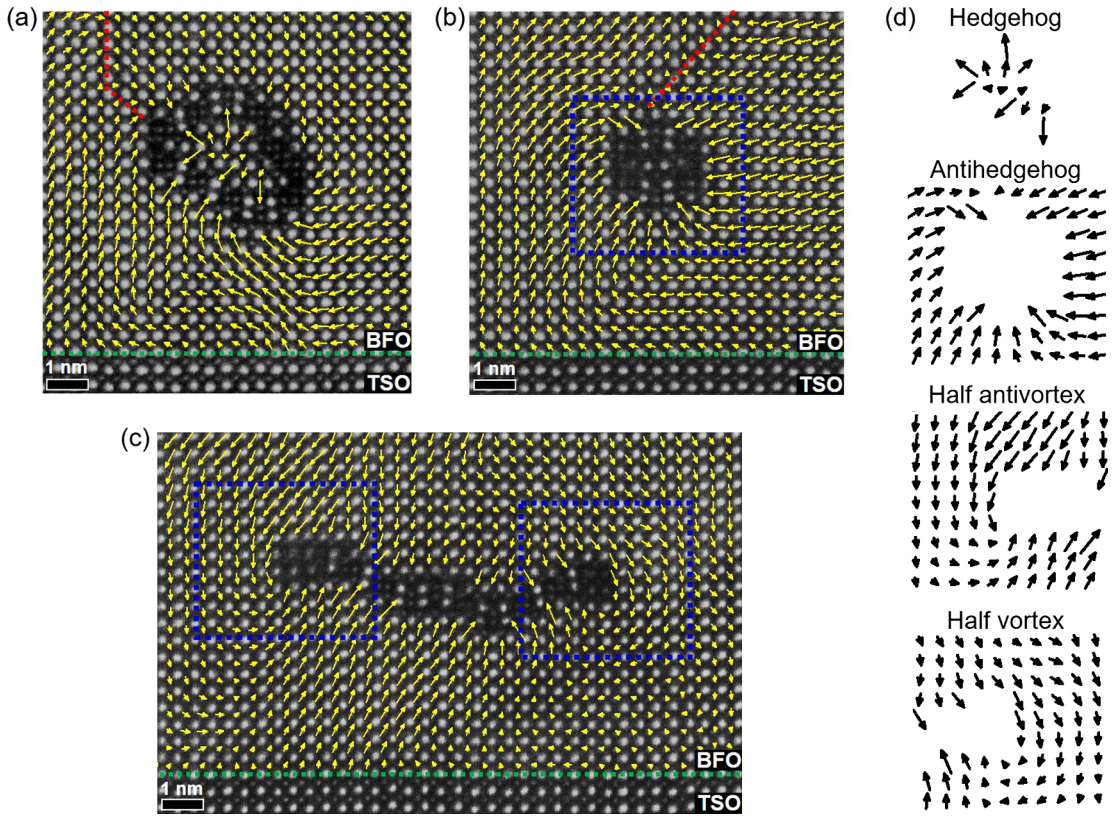

FIG. 4. Polarization maps of nanodomains induced by three different defects in the $BiFeO_3$ thin film. (a)–(c) HAADF STEM images of three different defects above the $BiFeO_3$(BFO)/$TbScO_3$(TSO) interface, where the polarization vectors ($-\boldsymbol{D}_{\mathbf{FB}}$, shown by yellow arrows) are overlaid on the $BiFeO_3$ lattice. The dashed red line marks the domain walls that penetrate to the top surface of the thin film. (d) Magnified map of the polarization vectors in the nanoregion enclosed by the loop defect in (a) and in the three different nanoregions highlighted by the blue rectangles in (b) and (c).

nanodomains in relatively thick ferroelectric films, which can overcome the limit on domain size or density imposed by the scaling law that states the domain width is proportional to the square root of the sample's thickness [29,30]. The polarization component perpendicular to the hedgehog plane (the image plane in our study) may be switchable. Therefore, further study of the electrical and magnetoelectric properties and dynamics under applied fields may assist future development of nanoelectronic devices such as high-density memories. On the other hand, it is well known that defect engineering through adding small amounts of donor dopant to a ceramic can create randomly oriented defect dipoles between donors and cation vacancies in the crystal structure, which promotes domain wall motion leading to enhanced piezoelectric properties [31]. Here, the antihedgehog polarization states stabilized by the nanoscale impurity defects possess mixed-phase structures that are reminiscent of the ferroelectric domains near a morphotropic phase boundary. These states may also exhibit enhanced properties such as giant piezoelectricity and thus are potentially attractive for electromechanical applications.

As it is known that nonstoichiometric phases can commonly occur in functional oxides due to different mechanisms, such as cation doping [24,25], stoichiometric fluctuation [21], and temperature variation during film growth [22], our observation of topological states induced by NSNRs in $BiFeO_3$ should stimulate efforts to design functional patterns of ferroelectric or multiferroic nanodomains or nanopolymorphs with a focus on controlling the intrinsic defect structures and motivate a search for a similar mechanism in other functional oxide systems. While conventional chemical engineering methods (composition tuning) and interface engineering methods (boundary condition tuning) produce only structure changes uniformly distributed within the whole material, defect engineering can generate functional structures at local nanoregions without the disruption of the bulk structural patterns, which is desirable as the dimensions of individual elements in nanodevices continue to shrink. Further developments may allow the NSNRs to be introduced in a fine controlled fashion, enabling their configurations to be adjusted during material synthesis, or allow the charge states of the NSNRs to be modified by external charge injection methods, opening the door to the control of nanodomain structures and the customized creation of topological states in complex materials through defect engineering.

The experimental work was mainly supported by the Department of Energy (DOE) under Grant No. DESC0014430 (L. Z. L., J. R. J., P. G., and X. Q. P.) and partially by the National Science Foundation (NSF) under Grants No. DMR-1420620 and No. DMR-1506535. The TEM used for this work was funded by the National Science Foundation under Grant No. DMR0723032, and by the University of California-Irvine's Materials Research Institute (IMRI). The theoretical component of this work at the Pennsylvania State University was supported by the U.S. Department of Energy, Office of Basic Energy Sciences, Division of Materials Sciences and Engineering under Award No. FG0207ER46417 (X. X. C. and L. Q. C.). Calculations at the Pennsylvania State University were performed on the Cyberstar Linux Cluster funded by the National Science Foundation through Grant No. OCI0821527. The work at Cornell University was supported by the National Science Foundation (Nanosystems Engineering Research Center for Translational Applications of Nanoscale Multiferroic Systems) under Grant No. EEC-1160504 (C. A., C. H., and D. G. S.). The authors also acknowledge the National Center for Electron Microscopy at Lawrence Berkeley National Laboratory for their support under DOE Grant No. DEAC0205CH11231 for user facilities. This work was performed in part at the Cornell Nanoscale Facility, a member of the National Nanotechnology Coordinated Infrastructure (NNCI), which is supported by the National Science Foundation (Grant No. ECCS-1542081). The authors also acknowledge Ramamoorthy Ramesh at University of California–Berkeley for discussing the results and providing insightful comments.

*Corresponding author.
xiaoqing.pan@uci.edu

[1] J. Seidel, *Topological Structures in Ferroic Materials Domain Walls*, Vortices and Skyrmions preface (Springer, New York, 2016).
[2] A. Wachowiak *et al.*, Science **298**, 577 (2002).
[3] S. Y. Xu *et al.*, Nat. Phys. **8**, 616 (2012).
[4] X. Z. Yu, Y. Onose, N. Kanazawa, J. H. Park, J. H. Han, Y. Matsui, N. Nagaosa, and Y. Tokura, Nature (London) **465**, 901 (2010).
[5] S. Heinze, K. von Bergmann, M. Menzel, J. Brede, A. Kubetzka, R. Wiesendanger, G. Bihlmayer, and S. Blügel, Nat. Phys. **7**, 713 (2011).
[6] T. Schulz, R. Ritz, A. Bauer, M. Halder, M. Wagner, C. Franz, C. Pfleiderer, K. Everschor, M. Garst, and A. Rosch, Nat. Phys. **8**, 301 (2012).
[7] F. Jonietz *et al.*, Science **330**, 1648 (2010).
[8] C. T. Nelson *et al.*, Nano Lett. **11**, 828 (2011).
[9] Y. L. Tang *et al.*, Science **348**, 547 (2015).
[10] A. K. Yadav *et al.*, Nature (London) **530**, 198 (2016).
[11] Y. Nahas, S. Prokhorenko, L. Louis, Z. Gui, I. Kornev, and L. Bellaiche, Nat. Commun. **6**, 8542 (2015).
[12] J. W. Hong, G. Catalan, D. N. Fang, E. Artacho, and J. F. Scott, Phys. Rev. B **81**, 172101 (2010).
[13] L. Z. Li, Y. Zhang, L. Xie, J. R. Jokisaari, C. Beekman, J.-C. Yang, Y.-H. Chu, H. M. Christen, and X. Pan, Nano Lett. **17**, 3556 (2017).
[14] L. Xie *et al.*, Adv. Mater. **29**, 1701475 (2017).
[15] F. Zavaliche, S. Y. Yang, T. Zhao, Y. H. Chu, M. P. Cruz, C. B. Eom, and R. Ramesh, Phase Transitions **79**, 991 (2006).
[16] Y. H. Chu, L. W. Martin, M. B. Holcomb, and R. Ramesh, Mater. Today **10**, 16 (2007).
[17] G. Catalan and J. F. Scott, Adv. Mater. **21**, 2463 (2009).
[18] R. R. Das *et al.*, Appl. Phys. Lett. **88**, 242904 (2006).
[19] F. Kubel and H. Schmid, Acta Crystallogr. Sect. B **46**, 698 (1990).
[20] L. Z. Li, P. Gao, C. T. Nelson, J. R. Jokisaari, Y. Zhang, S.-J. Kim, A. Melville, C. Adamo, D. G. Schlom, and X. Pan, Nano Lett. **13**, 5218 (2013).
[21] H. Deniz, A. Bhatnagar, E. Pippel, R. Hillebrand, A. Hähnel, M. Alexe, and D. Hesse, J. Mater. Sci. **49**, 6952 (2014).
[22] J. F. Ihlefeld *et al.*, Appl. Phys. Lett. **92**, 142908 (2008).
[23] See Supplemental Material at http://link.aps.org/supplemental/10.1103/PhysRevLett.120.137602 for transmission electron microscopy and phase-field simulation methods, and discussion on strain effects of defects.
[24] I. MacLaren *et al.*, Appl. Mater. **1**, 021102 (2013).
[25] I. MacLaren *et al.*, Appl Mater. **2**, 066106 (2014).
[26] R. J. Zeches *et al.*, Science **326**, 977 (2009).
[27] Y.-M. Kim, A. Morozovska, E. Eliseev, M. P. Oxley, R. Mishra, S. M. Selbach, T. Grande, S. T. Pantelides, S. V. Kalinin, and A. Y. Borisevich, Nat. Mater. **13**, 1019 (2014).
[28] Y.-M. Kim, J. He, M. D. Biegalski, H. Ambaye, V. Lauter, H. M. Christen, S. T. Pantelides, S. J. Pennycook, S. V. Kalinin, and A. Y. Borisevich, Nat. Mater. **11**, 888 (2012).
[29] C. W. Huang, L. Chen, J. Wang, Q. He, S. Y. Yang, Y. H. Chu, and R. Ramesh, Phys. Rev. B **80**, 140101 (2009).
[30] Y. B. Chen, M. B. Katz, X. Q. Pan, R. R. Das, D. M. Kim, S. H. Baek, and C. B. Eom, Appl. Phys. Lett. **90**, 072907 (2007).
[31] C. H. Hong *et al.*, J. Mater. **2**, 1 (2016).

Supporting Information

Defect-induced hedgehog polarization states in multiferroics

Linze Li,[1,2] Xiaoxing Cheng,[3] Jacob R. Jokisaari,[2] Peng Gao,[2] Jason Britson,[3] Carolina Adamo,[4] Colin Heikes,[4] Darrell G. Schlom,[4,5] Long-Qing Chen,[3] and Xiaoqing Pan[1,6]*

[1]Department of Chemical Engineering and Materials Science, University of California - Irvine, Irvine, CA 92697, USA

[2]Department of Materials Science and Engineering, University of Michigan, Ann Arbor, Michigan 48109, USA

[3]Department of Materials Science and Engineering, Penn State University, University Park, PA 16802, USA

[4]Department of Materials Science and Engineering, Cornell University, Ithaca, New York 14853, USA

[5]Kavli Institute at Cornell for Nanoscale Science, Ithaca, New York 14853, USA

[6]Department of Physics and Astronomy, University of California - Irvine, Irvine, CA 92697, USA

*Correspondence to: xiaoqing.pan@uci.edu

METHODS

Transmission electron microscopy (TEM). Cross-sectional TEM samples were prepared by the conventional grinding, polishing and ion milling process. First, the cross-sectional sample was polished to a thickness of ~20-30 μm in wedge shape using a tripod polisher. After mechanical polishing, the sample was further milled to electron transparency by a Gatan Precision Ion Polishing System 2, with an ion gun voltage = 4 kV and angle = ±4°. At the final step of ion milling, a voltage of 0.1 kV was used to remove any amorphous layer on the surface. Dark-field diffraction-contrast imaging was performed using a JEOL 3011 operated at 300 kV. STEM HAADF experiments were carried out on a FEI Titan 80-300 microscope at the National Center for Electron Microscopy of Lawrence Berkeley National Laboratory (LBNL). The microscope is equipped with double aberration correctors and its resolution in STEM mode is ~0.5 Å. The accelerating voltage, convergence angle of the incident electrons, and the collection angle for HAADF imaging are 300 kV, 29 mrad and 79-200 mrad, respectively. Atomic displacement $\boldsymbol{D_{FB}}$ vectors were directly measured from the STEM HAADF images by fitting each image with a series of two-dimensional (2D) Gaussian functions. After fitting, the atomic positions were extracted from the centers of these 2D Gaussian functions.

Phase field simulations. A FORTRAN code based on the phase-field model was employed to simulate the evolution of the spatial polarization as a function of time, as described by the time-dependent Ginzburg-Landau equation:

$$\frac{\partial P_i(x,t)}{\partial t} = -L\frac{\delta F}{\delta P_i(x,t)}, i = 1,2,3$$

in which P is the primary order parameter (polarization), F is the total free energy including landau, elastic, electrostatic, and gradient energies, and L is a kinetic parameter related to domain wall mobility.

$$F = \int_V [f_{Landau}(P_i) + f_{Elastic}(P_i, \epsilon_{ij}) + f_{Electric}(P_i, E_i) + f_{Gradient}(P_{i,j})]dV$$

We performed a 2D simulation in the x-z plane with a system size of 51.2 nm × 50 nm, where the thickness of the substrate was 8 nm and film was 40 nm. The Landau, elastic, and electrostrictive coefficients used are listed in Table S1. The elastic boundary condition was chosen to be traction free on film surface, and zero displacement at the substrate (bottom of the

simulation region). Since in experiment, there was no bottom electrode, we chose to use the open circuit electric boundary condition, for which the electric displacement was fixed at 0 at the film/substrate interface and film surface. We employed an isotropic gradient energy coefficient of $g_{11} = 1$ and an isotropic dielectric constant of $\epsilon_{ii} = 50$. For most simulations (except for the simulations in Fig. S6 (a,b)), the initial condition is set to random noise; for the simulations in Fig. S6 (a,b), in order to study the interaction of the bulk domain wall and the charged defect, the initial condition included a 109˚ domain wall in Fig. S6a, and a 180˚ domain wall in Fig. S6b terminated at the defect.

Strain effects of the defects

Using the linear defect as an example (Fig. S6(c) and Fig. S8 to S11), we show that the strain induced by this defect has minimal effect on the polarization distribution. Similar to the analysis of the case of the semi-circular loop defect shown in Fig. S4, geometric phase analysis (GPA) of the case of the linear defect in Fig. S8 also shows little strain in the $BiFeO_3$ matrix surrounding this defect. Since the defect and $BiFeO_3$ have different atomic structures, GPA cannot be used to determine the strain at the defect or at the defect/$BiFeO_3$ boundary. Therefore, we estimated the defect-induced strain by directly measuring the lattice spacing of the atomic structures (Fig. S9 and S10). The measurements show a low compressive strain (e_{yy} ~-2%) along the vertical direction at the defect (Fig. S9), and a large shear strain (e_{yz} ~ -16%) along the horizontal direction (Fig. S10). We performed phase field simulations to examine the effect of the strain on the polarization. With identical charge conditions as the case shown in Fig. S6c, we apply additional compressive strain (e_{yy} ~ -5%) or shear strain (e_{yz} ~ -20%) to the same defect configuration. The corresponding simulated polarization patterns are shown in Fig. S11, (a) and (b), respectively, where the polarization vectors are overlaid on the color map of strain distribution. The large shear strain at the defect is relaxed to less than 5% in the nearby $BiFeO_3$ lattice, consistent with the low strain measured in $BiFeO_3$ by the STEM imaging. The difference in the polarization distribution between the strained conditions and the zero strain case is almost indistinguishable; suggesting that the defect-induced strain has a negligible effect on the polarization state.

Landau coefficient	**Elastic constant**	**Electrostrictive coefficient**
a1=4.64385*81(T-1103k)*10^5 ($C^{-2}m^2N$)	c11=2.28*10^11 (Nm^{-2})	Q11=0.032 ($C^{-2}m^4$)
a11=2.29047*10^8 ($C^{-4}m^6N$)	c12=1.28*10^11 (Nm^{-2})	Q12=-0.016 ($C^{-2}m^4$)
a12=3.06361*10^8 ($C^{-4}m^6N$)	c44=6.6*10^10 (Nm^{-2})	Q44=0.02015 ($C^{-2}m^4$)
a111=5.99186*10^7 ($C^{-6}m^{10}N$)		
a112=-3.3398*10^5 ($C^{-6}m^{10}N$)		
a123=-1.77754*10^8 ($C^{-6}m^{10}N$)		

Table S1. Coefficients used in the phase-field simulation.

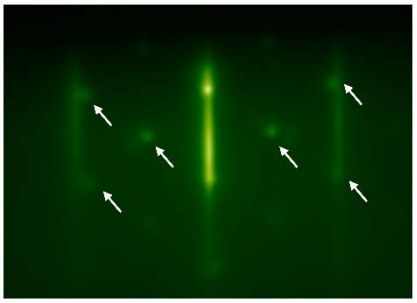

Figure S1. RHEED patterns collected during film growth. The streaks are associated with $BiFeO_3$ and the additional spots (indicated by the arrows) can be indexed to diffraction from (111)-oriented γ-Fe_2O_3.

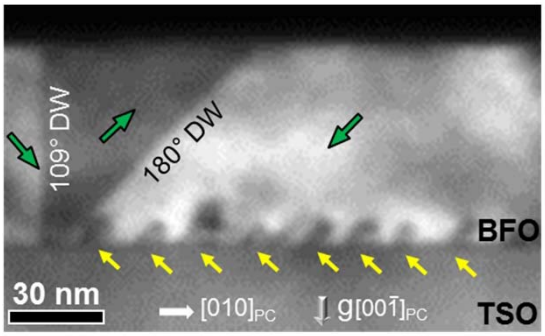

Figure S2. Cross-sectional dark-field TEM image of the $BiFeO_3$ (BFO) thin film grown on a $TbScO_3$ (TSO) substrate, showing a triangular 109°/180° domain wall (DW) junction in the bulk film and a high-density array of nanodomains (indicated by the yellow arrows) above the $BiFeO_3/TbScO_3$ interface. These nanodomains are introduced by the array of defects observed in Figure 1c.

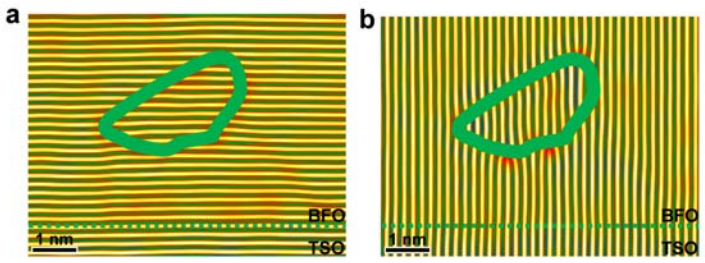

Figure S3. (a) The same HAADF STEM image as Fig. 2(a) filtered in Fourier space by including only the $00h_{PC}$ diffraction frequencies. (b) The same HAADF STEM image filtered in Fourier space by including only the $0h0_{PC}$ diffraction frequencies.

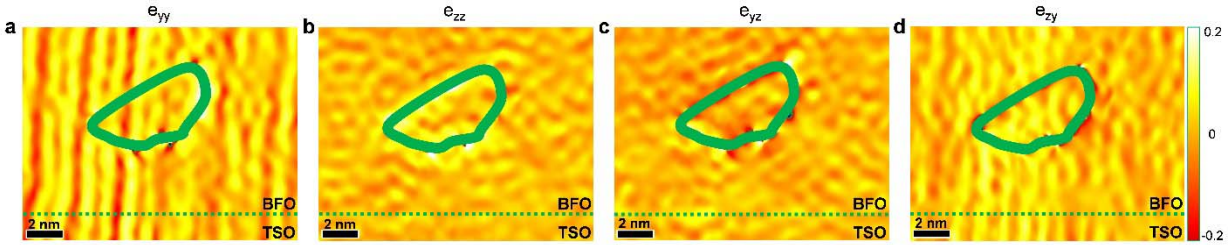

Figure S4. (a-d) Geometric phase analysis (GPA) of the HAADF STEM images reveals the strain in the $BiFeO_3$ lattice surrounding the semi-circular loop defect. Note that the striped patterns in (a) are caused by scanning noise in the STEM image.

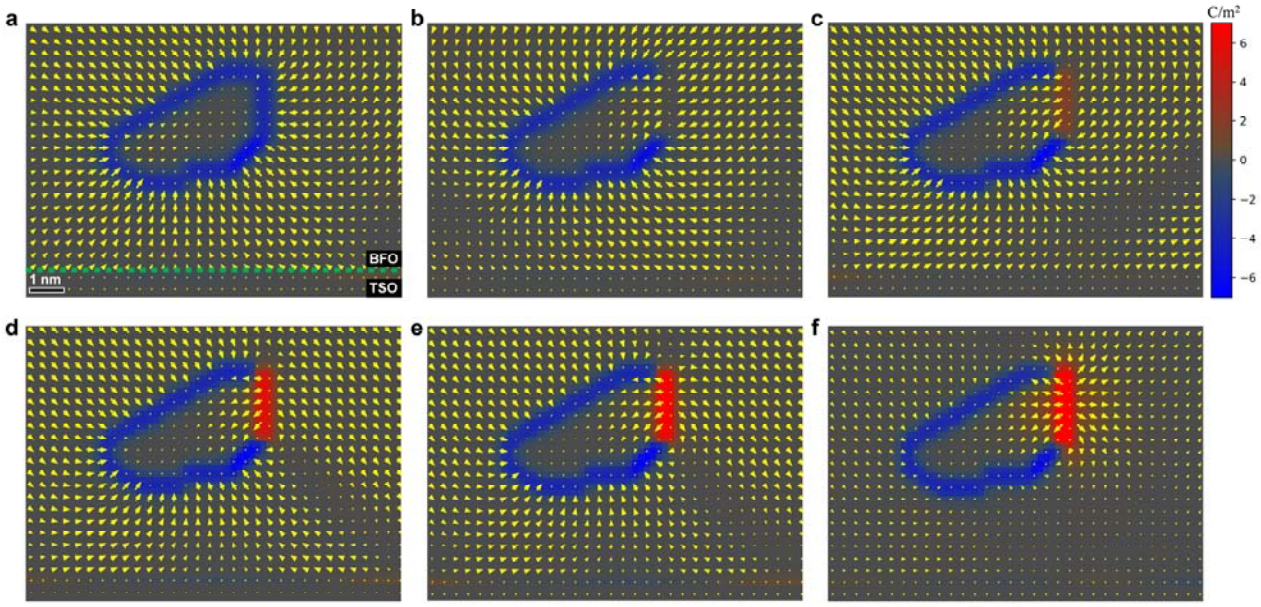

Figure S5. (a-f) Phase field simulation of polarization distribution in the image plane of the domain structure stabilized by a charged defect with the configuration same to Fig. 3(b) and the same negative charge density of -1.1 C/m^2 applied to the left curved/inclined part, but with different charge densities (a, -1.1 C/m^2; b, 0 C/m^2; c, +0.55 C/m^2; d, +1.1 C/m^2; e, +2.2 C/m^2; and f, +5.5 C/m^2) applied to the right-side vertical segment. The polarization vectors are overlaid on a color map of the charge distribution. The result in (d) with the charge density of +1.1 C/m^2 on the right-side segment is most consistent to the experimental observation.

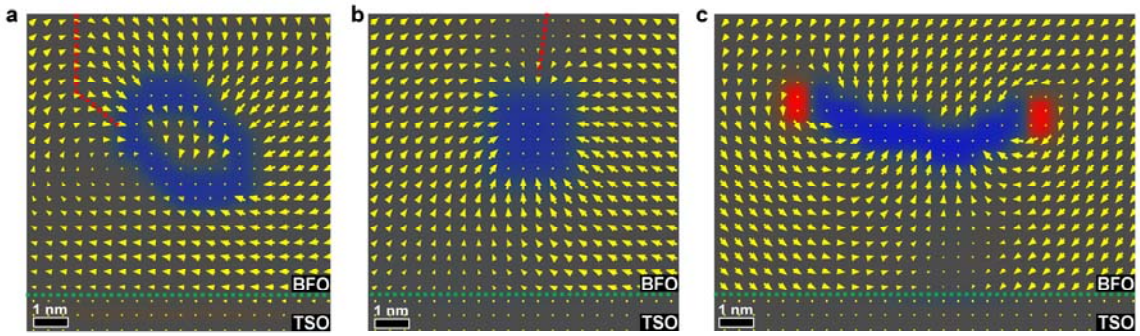

Figure S6. (a-c) Phase field simulation of polarization distribution in the image plane of the domain structures stabilized by three different charged defects with configurations similar to the experimental observations in Fig. 4(a)-(c). The polarization vectors are overlaid on a color map of the charge distribution, where red, blue, and gray colors represent positive (+1.1 C/m^2), negative (-1.1 C/m^2), and zero charge densities, respectively. These simulated polarization structures surrounding the charged defects generally follow the experimental observations, forming antihedgehog states and vortex domains in (a) and (b) and semi-antivortex at the left edge of the defect in (c). The particular polarization rotation patterns at the simulated vortices, however, do not exactly match the experimental results. The differences could be attributed to the uniform charge density assumed in the simulation, as the charge distribution along the defects should be non-uniform in reality due to local charge compensation by the mobile carriers or oxygen vacancies. Such a non-uniform charge density should alter the polarization structures.

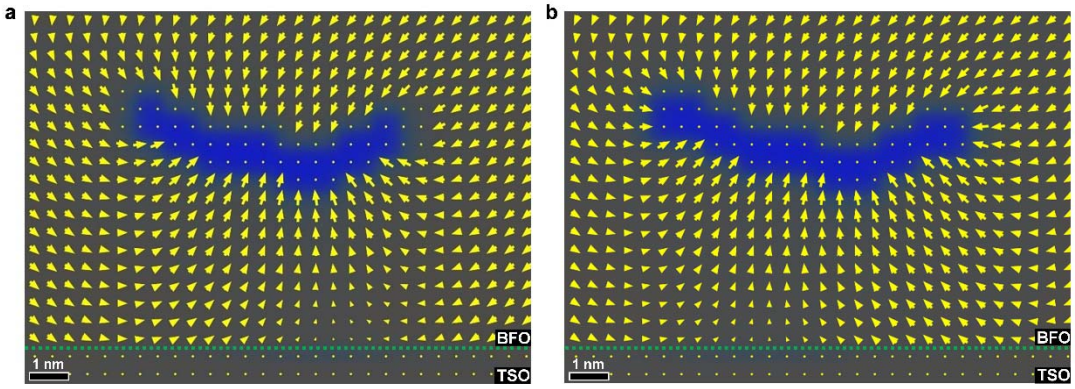

Figure S7. Phase field simulation of the polarization distribution in the image plane of the domain structure stabilized by a charged defect with a configuration identical to the case in Fig. S6(c), but with different charge distributions: (a) no charge and (b) negative charge at the two edges of the linear defect. The polarization vectors are overlaid onto the color maps of the charge distribution, where the blue and gray color represent the negative (-1.1 C/m^2) and zero charge densities, respectively. In both cases, the polarization semi-vortex or semi-antivortex does not form at either of the two defect edges, which differs from the experimental observation in Figure 4c.

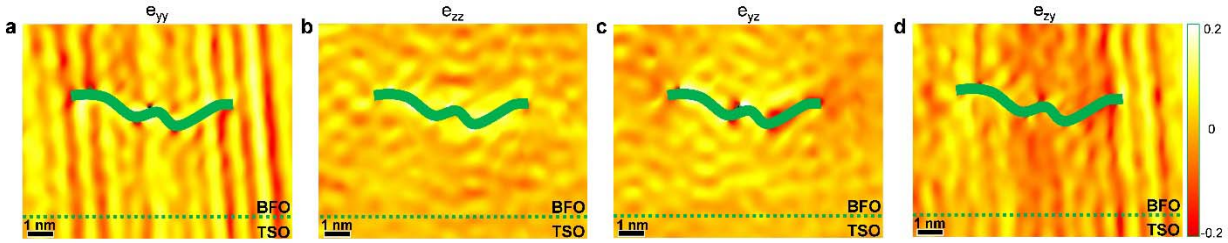

Figure S8. (a-d) Geometric phase analysis (GPA) of the HAADF STEM images shows the lack of strain in the $BiFeO_3$ lattice surrounding the linear defect. Note that the striped patterns in (a) and (d) are caused by scanning noises of the STEM image.

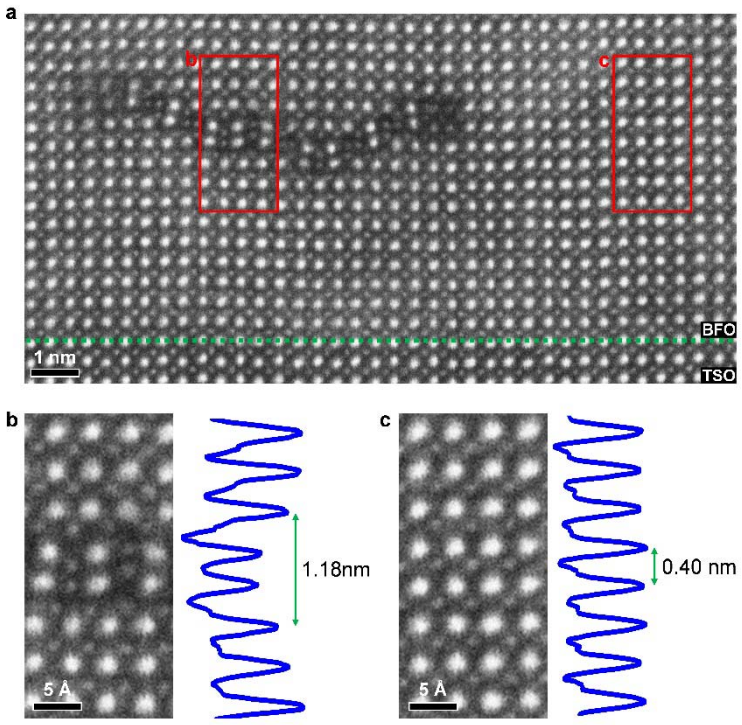

Figure S9. Analysis of out-of-plain strain (e_{zz}) of the linear defect. (a) HAADF STEM image of the $BiFeO_3/TbScO_3$ (BFO/TSO) interface region containing the linear defect. (b) Magnified image of the planar unit of the defect (red rectangular highlighted region "b" in (a)) and the corresponding averaged intensity line profile on the right. The measured thickness of the defect is 1.18 nm. (c) Magnified image of a nanoregion in the $BiFeO_3$ matrix and the corresponding averaged intensity line profile on the right. The measured out-of-plane lattice constant of $BiFeO_3$ is 0.40 nm. Since the defect is inserted into the $BiFeO_3$ matrix, replacing three pseudocubic unit cells, there should be a small compressive strain (e_{zz}~ -0.02) at the defect.

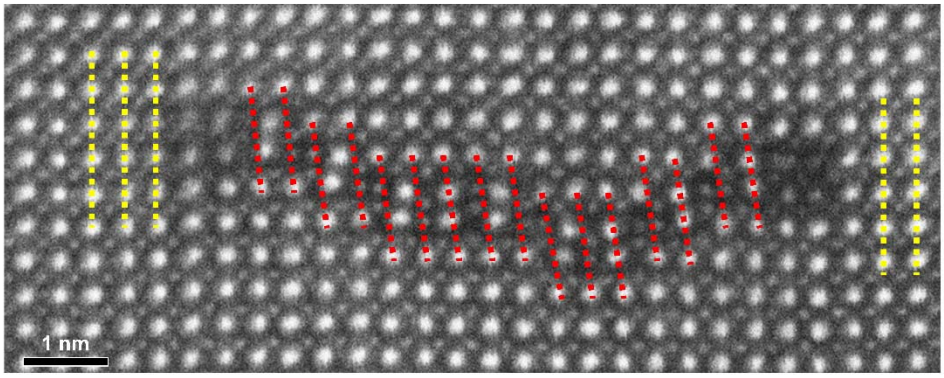

Figure S10. Analysis of the shear strain (e_{yz}) at the linear defect. HAADF STEM image of the linear defect shows the atomic shifts of the $BiFeO_3$ lattice across the defect leads to a large shear strain ($e_{yz} \sim -0.16$) between the top and the bottom boundaries of the defect.

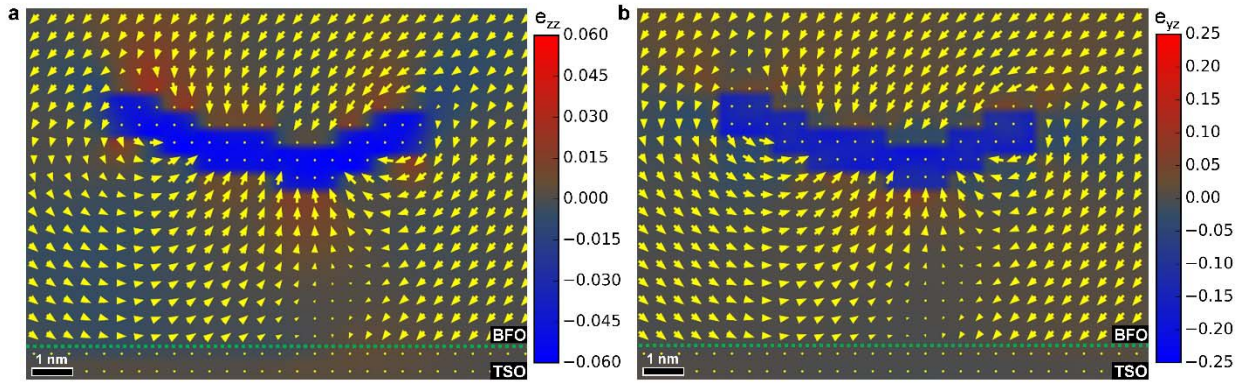

Figure S11. Assessment of the influence of the defect-induced strain on the polarization distribution around the linear defect. Phase field simulation of the polarization distribution in the image plane of the domain structure stabilized by a charged defect with a configuration and charge distribution identical to the case in Fig. S6(c), but with an added eigenstrain of (a) e_{zz} of -0.05 or (b) e_{yz} of -0.20. The color represents e_{zz} in (a) and e_{yz} in (b).